nature communications

Article

https://doi.org/10.1038/s41467-024-54998-1

Transition metal vacancy and position engineering enables reversible anionic redox reaction for sodium storage

Received: 19 September 2023

Accepted: 26 November 2024

Published online: 02 January 2025

Check for updates

Congcong Cai[1,5], Xinyuan Li[1,5], Jiantao Li[2,5] ✉, Ruohan Yu[1,5], Ping Hu[1], Ting Zhu[1], Tianyi Li[3], Sungsik Lee[3], Nuo Xu[1], Hao Fan[1], Jinsong Wu[1], Liang Zhou[1] ✉, Liqiang Mai[1] ✉ & Khalil Amine[2,4] ✉

Triggering the anionic redox reaction is an effective approach to boost the capacity of layered transition metal (TM) oxides. However, the irreversible oxygen release and structural deterioration at high voltage remain conundrums. Herein, a strategy for Mg ion and vacancy dual doping with partial TM ions pinned in the Na layers is developed to improve both the reversibility of anionic redox reaction and structural stability of layered oxides. Both the Mg ions and vacancies (□) are contained in the TM layers, while partial Mn ions (~1.1%) occupy the Na-sites. The introduced Mg ions combined with vacancies not only create abundant nonbonding O 2*p* orbitals in favor of high oxygen redox capacity, but also suppress the voltage decay originated from Na–O–□ configuration. The Mn ions pinned in the Na layers act as "rivets" to restrain the slab gliding at extreme de-sodiated state and thereby inhibit the generation of cracks. The positive electrode, $Na_{0.67}Mn_{0.011}[Mg_{0.1}□_{0.07}Mn_{0.83}]O_2$, delivers an enhanced discharge capacity and decent cyclability. This study provides insights into the construction of stable layered oxide positive electrode with highly reversible anionic redox reaction for sodium storage.

Sodium-ion batteries (SIBs) represent an alternative candidate for large-scale energy storage to lithium-ion batteries owing to their low cost[1–3]. However, their unsatisfactory electrochemical performances hinder the practical application due to the lack of suitable cathode materials[4–7]. As a family of cathode materials, layered transition metal oxides (Na_xTMO_2, TM represents transition metal) have attracted increasing interest for their relatively high theoretical capacities and efficient two-dimensional Na^+ diffusion paths[8–11]. However, the capacity of conventional cathode materials, which is determined by the cationic redox of TMs, is gradually approaching the theoretical limit. Fortunately, the discovery of anionic redox reaction provides a new opportunity to construct layered oxides with high capacities beyond the limit of TM redox[12–15].

The anionic (oxygen) redox reaction of Na_xTMO_2 is similar to that of Li-rich Mn-based oxides. The existence of nonbonding O 2*p* states is generally recognized to be the origin of anionic redox reaction[16,17]. For instance, the partial substitution of TMs by Li in Li-rich oxides induces the formation of Li–O–Li configuration, which enables the lone-pair O 2*p* state generation on account of the weak overlap between O 2*p* and Li 2*s* orbitals[18,19]. Analogously, such a situation can also be realized in Na_xTMO_2 by constructing the Na–O–X paradigms. Apart from Na–O–Li[20,21], Na–O–X configurations can also be Na–O–Mg[22,23], Na–O–Zn[24,25], and even Na–O–vacancy (□)[26–28]. The X–O bonds are so weak that the O 2*p* band is close to the Fermi level (E_f), which facilitates the oxygen redox reaction. Among them, the Na–O–□ configuration

[1]State Key Laboratory of Advanced Technology for Materials Synthesis and Processing, Wuhan University of Technology, Wuhan 430070, China. [2]Chemical Sciences and Engineering Division, Argonne National Laboratory, Lemont, IL 60439, USA. [3]X-ray Science Division, Advanced Photon Source, Argonne National Laboratory, Lemont, IL 60439, USA. [4]Pritzker School of Molecular Engineering, The University of Chicago, Chicago, IL 60637, USA. [5]These authors contributed equally: Congcong Cai, Xinyuan Li, Jiantao Li, Ruohan Yu. ✉e-mail: jiantao_work@126.com; liangzhou@whut.edu.cn; mlq518@whut.edu.cn; amine@anl.gov

induced anionic redox reaction exhibits a high voltage plateau with low hysteresis, and the existence of vacancies endows the material with high structural flexibility. Although the anionic redox combined with cationic redox reaction in layered compounds brings about a staggering capacity increase, the irreversible oxygen release and voltage decay limit the application. For example, Hu et al. reported a $Na_{0.653}[Mn_{0.929}\square_{0.071}]O_2$ material by replacing partial Mn sites with vacancies and a noticeable potential plateau (~4.2 V *vs.* Na^+/Na) from the oxygen redox reaction of Na–O–□ could be observed[29]. The obtained material delivered a high capacity but with considerable voltage decay during subsequent cycling. Huq et al. developed a $Na_{4/7}[Mn_{6/7}\square_{1/7}]O_2$ material with native vacancies, which exhibited similar voltage decay[26]. Moreover, the oxygen redox is normally triggered at high potential (>4.1 V *vs.* Na^+/Na), where the extraction of most Na^+ from interlayers increases the repulsion of oxygen layers and deteriorates the structural stability. Therefore, for layered oxides with anionic redox reactions, synergistically enhancing the activity of anionic redox reaction and structural stability is still a great challenge.

Considering the ability of Mg doping in introducing Na–O–Mg configuration for anionic redox and enhancing the structural stability, we developed a Mg ion and vacancy dual doping strategy for layered oxides in this study, which enables simultaneous improvement in oxygen redox activity and structural stability. The introduced Mg ions combined with vacancies not only create abundant nonbonding O 2*p* orbitals in favor of high oxygen redox capacity but also suppress the voltage decay originated from the Na–O–□. Partial occupancy of Mn ions (~1.1%) in Na-sites has been identified by scanning transmission electron microscopy (STEM). Various ex/in situ analyses demonstrate that the mis-occupied Mn ions can act as "rivets" to restrain the slab gliding at the deep de-sodiated state and thereby inhibit the generation of cracks. Consequently, the obtained P2-type $Na_{0.67}Mn_{0.011}[Mg_{0.1}\square_{0.07}Mn_{0.83}]O_2$ cathode material demonstrates a significantly improved capacity of 155.1 mAh g^{-1} at 14 mA g^{-1} and decent cyclability with 87.5% capacity retention over 200 cycles at 140 mA g^{-1}. Density functional theory (DFT) calculations reveal that the Mg ion and vacancy dual doping enhances the anionic redox activity and structural stability of the layered oxide cathode. This contribution sheds light on the design of stable layered oxides with highly reversible anionic redox reactions for high-energy SIBs.

Results

Structural characterizations

A series of $Na_{0.67}Mg_xMn_{1-x}O_2$ ($x = 0–0.2$) materials were synthesized by a facile organic acid-assisted solid state reaction. The chemical composition of the as-prepared materials is determined by inductively coupled plasma-optical emission spectrometer (ICP-OES, Supplementary Table 1). The Na/Mn ratio of the pristine compound without Mg doping (denoted as NMV) is 0.685:0.895. Ideally, the TM layers should be fully occupied by transition metals, implying there are ~10% vacancies in the TM layers. After the introduction of 10% Mg, the sample (denoted as NMV-M10) has a Na/Mn/Mg ratio of 0.671:0.836:0.097, indicating there are still vacancies existing.

The crystal structures of the samples are studied by X-ray diffraction (XRD) and Rietveld refinement. With the increasing of Mg content from 0 to 20%, a structure evolution from P′2/P2 mixed phase to P2 phase can be observed (Supplementary Fig. 1a), suggesting the Mg^{2+} substitution effectively alleviates the structural distortion during synthesis process. When the Mg content increases from 0 to 10%, the (002) peak shifts to a lower position (Supplementary Fig. 1b), indicating an expansion of the unit cell along the *c*-axis. This shift is due to the larger ionic radius of Mg ions compared to Mn ions, which increases the TM layer thickness. If Mg ions were to occupy the sodium layers, the smaller radius of Mg^{2+} compared to Na^+ would reduce the interlayer distance, causing the *c*-axis to shrink[9]. However, this is contrary to the observed results. Therefore, the introduced Mg ions in NMV-M10 are more likely to occupy the transition metal layers. According to the Rietveld refinement results, the pristine NMV adopts mixed phases of orthorhombic lattice with the *Cmcm* space group (P′2 structure, 15.57%) and hexagonal lattice with the *P*63/*mmc* space group (P2 structure, 84.43%) (Supplementary Fig. 2). The P′2 structure is considered as a distorted phase (Supplementary Fig. 3) due to the presence of Jahn–Teller active Mn^{3+}[30], which will be discussed further in the following part. With the introduction of 10% Mg, the obtained NMV-M10 adopts a pure P2 phase (Fig. 1a). The low agreement factors indicate the reliable refinement results. According to the refinement results (Supplementary Table 2), the Mg ions occupy the TM-sites, while ~1.1% of Na_e sites are occupied by Mn ions. Such a trace amount of TM ions occupying in sodium layers should not cause the dramatically decreased interlayer distance. The total occupancy of TM-sites suggests the existence of a significant amount of TM vacancies. According to the Rietveld refinement results, the schematic crystal structure of NMV-M10 is provided in Fig. 1b. Moreover, the appearance of diffraction peaks at 19–24° indicates the existence of superstructure in the samples (Supplementary Fig. 1c). The NMV shows superstructural peaks at 19.7 and 20.1°, demonstrating the formation of a ribbon-ordered superstructure of Mn and vacancy within the TM layers. With the introduction of Mg, the original superstructural peaks disappear and a new diffraction appears at 22.2°, suggesting the transformation of superstructure into a honeycomb-ordered superstructure of Mn and Mg/vacancy[12]. When the Mg content exceeds 10%, the MnO_2 impurity phase can be observed (Supplementary Fig. 1a), suggesting the up limit for Mg doping.

X-ray photoelectron spectroscopy (XPS) is conducted to determine the valence states of Mn (Supplementary Fig. 4). For NMV, the peaks at ~642 and ~654 eV can be assigned to the Mn $2p_{3/2}$ and $2p_{1/2}$ components, respectively. With the introduction of Mg, the Mn 2*p* XPS peaks slightly shift towards higher binding energy, indicating the formation of high-valence-state Mn^{4+} with partial substitution of Mn^{3+} with Mg^{2+}. Six-coordinated Mn^{3+} has an uneven distribution of electrons in its d-orbitals ($t_{2g}3–e_g1$). Specifically, the single electron in the e_g orbital leads to an uneven electron density distribution, causing the ion to distort to relieve this instability. This distortion, known as the Jahn-Teller distortion, typically results in an elongation or compression of the octahedral coordination environment, which weakens the structural stability of the material. The XPS results indicate that the Mg doping is beneficial for decreasing the amount of Mn^{3+} and alleviating the Jahn-Teller distortion of Mn^{3+}.

Scanning electron microscopy (SEM) characterization reveals that all the samples with different Mg contents are composed of micrometer crystals with sizes of 1–4 μm (Supplementary Fig. 5). To directly observe the atomic structure of NMV-M10, STEM with high-angle annular dark field (HAADF) and annular bright field (ABF) detectors are employed (Fig. 1c, d). The bright dots in HAADF-STEM (Fig. 1c) and the dark dots in ABF-STEM (Fig. 1d) are assigned to heavy TM atoms (Mn), while the bright dots in ABF-STEM correspond to the light atoms (Na, O, Mg). The staggered arrangement of TM and Na layers indicates that the NMV-M10 has a typical layered structure. It should be noted that some bright contrasts exist between adjacent TM layers in the HAADF image as indicated by red arrows and dark dots are observed at the same positions in the corresponding ABF image. The HAADF and ABF images demonstrate that a small fraction of Mn ions are located at the Na layers in NMV-M10 with local formation of spinel structures like $MgMn_2O_4$ or $NaMn_2O_4$[31]. Fast Fourier transformation (FFT, Fig. 1e) verifies the P2 structure and high crystallinity of NMV-M10. In the intensity line along the red rectangle in Fig. 1f, the Mn signal in Na layer can be well detected. Geometric phase analysis (GPA) is carried out to image the strain distribution of NMV-M10 (Supplementary Fig. 6). The mis-occupied Mn ions in Na sites exhibit drastic internal strain, which can be attributed to the strong interaction of lattice oxygen with the

https://doi.org/10.1038/s41467-024-54998-1

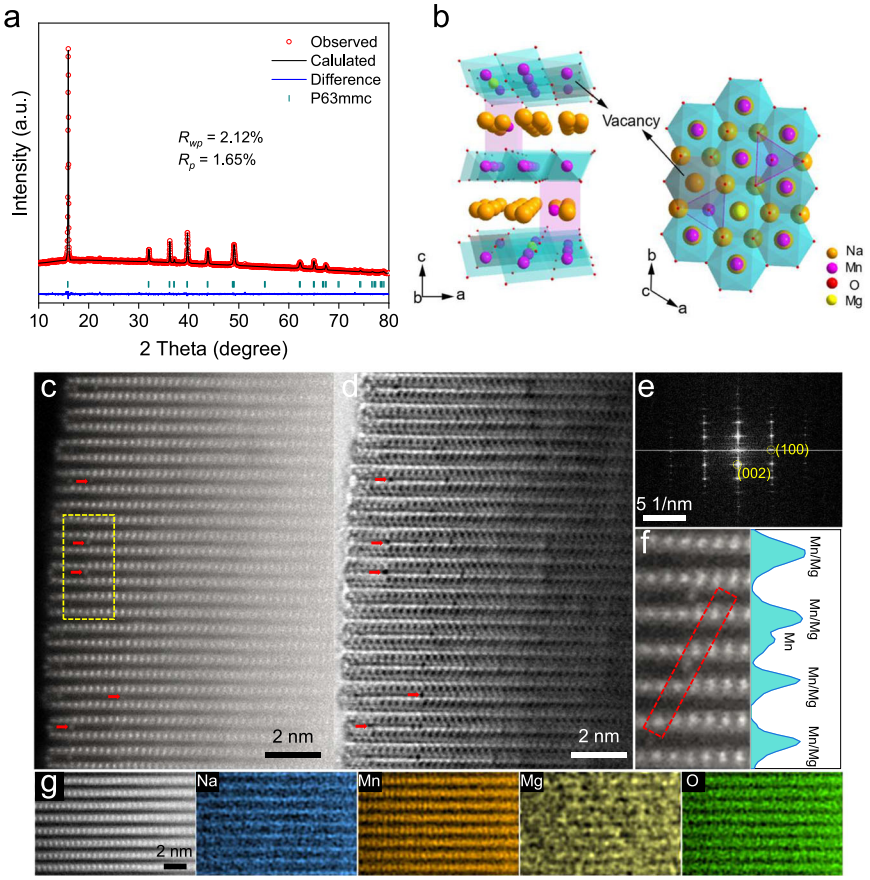

Fig. 1 | Structural characterizations of NMV-M10. a XRD Rietveld refinement; **b** Schematic crystal structure; **c** HAADF- and **d** ABF-STEM images, riveted Mn ions in sodium layers are marked with red arrows; **e** FFT image; **f** enlarged view of the marked region (yellow rectangle) in (**c**) and the intensity line profile extracted along the red rectangle; **g** atomic EDS-mappings.

mis-occupied Mn ions. Such mis-occupied TM ions in the Na layers can act as "rivets" to restrain the oxygen layer gliding when the Na^+ ions are extracted at high potential[32]. Atomic energy dispersive spectroscopy (EDS) mapping is conducted to reveal the elemental distribution in NMV-M10 (Fig. 1g). The TM layers and Na layers are distributed according to the P2 stacking structure and the Mg is distributed in the TM layers, suggesting the Mg preferentially substitutes the vacancies and Mn-sites in TM layers, agreeing well with the XRD results. For the pristine NMV, no Mn ions can be observed in the Na layers (Supplementary Fig. 7), suggesting that the occupation of Mn ions in Na-sites is induced by Mg doping. Moreover, vacancies can be clearly observed in the TM layers of NMV from the HAADF image (Supplementary Fig. 8). The Mn ions and vacancies are arranged into a ribbon-ordered superstructure, in well agreement with the XRD results[12].

Electrochemical performances

The electrochemical behaviors are evaluated in coin cells. The cyclic voltammetry (CV) curves of NMV and NMV-M10 are displayed in Fig. 2a. According to the redox potential, the CV profile of pristine NMV can be briefly separated into three regions. At 2.0–2.4 V (*vs.* Na^+/Na), the reduction/oxidation peaks are attributed to Mn^{3+}/Mn^{4+} redox; at 2.4–4.0 V, the multiple redox peaks are caused by the Mn^{3+}/Mn^{4+} redox induced structural ordering transitions during sodiation/desodiation[33–35]; at 4.0–4.35 V, the pair of sharp peaks are attributed to the oxygen redox of Na–O–□ configuration[26,29]. In contrast, the CV curves for NMV-M5 (Supplementary Fig. 9a) and NMV-M10 at 2.4–4.0 V are much smoother, suggesting the introduction of Mg disrupts the complex structural transitions and stabilizes the structure[33,34]. A pair of broaden peaks are observed at ~2.8 V after the introduction of Mg, which are associated with the oxygen redox of Na–O–Mg configuration[36]. This indicates that the Mg doping triggers the oxygen redox at a relatively low voltage and contributes to a high capacity. In addition, the reduction peaks at ~4.2 V from the oxygen redox of Na–O–□ configuration slightly weaken with the increasing of Mg content, and disappear completely in NMV-M20 (Supplementary Fig. 10). This phenomenon might be caused by the gradual occupation of TM vacancies by Mg ions.

The first five galvanostatic charge/discharge (GCD) profiles of NMV and NMV-M10 in the potential range of 2.0–4.35 V are displayed in Fig. 2b, c. The NMV-M10 delivers the highest capacity of 155.1 mAh g^{-1} at 14 mA g^{-1}, while the capacities for NMV and NMV-M5 are 138.6 and 133.9 mAh g^{-1} (Supplementary Fig. 9b), respectively. The NMV-M10 exhibits the smoothest GCD profiles and a reduced voltage plateau capacity at ~4.2 V (Fig. 2c), agreeing well with the CV results. The voltage plateau at ~4.2 V in NMV exhibits a rapid decay in subsequent cycles (Fig. 2b), which is caused by the irreversible anionic redox reactions of Na–O–□[29]. In contrast, this voltage decay can be well suppressed in NMV-M10 (Fig. 2c). The first discharge capacities of the samples at 14 mA g^{-1} with different Mg and vacancy contents can be divided into three parts: the capacities at 4.0–4.35 V and 2.4–4.0 V are ascribed to the anionic redox of Na–O–□ and Na–O–Mg configurations, respectively (Supplementary Fig. 11). And the capacity at 2.0–2.4 V is related to the cationic redox contribution. The NMV-M10 displays a lower anionic redox capacity from Na–O–□ than NMV, which is due to the partial occupation of vacancies by Mg^{2+}. This phenomenon can also be observed in P3-type $Na_{0.67}Mg_{0.2}Mn_{0.8}O_2$, which exhibits a short plateau at ~4.2 V but also decays in subsequent

https://doi.org/10.1038/s41467-024-54998-1

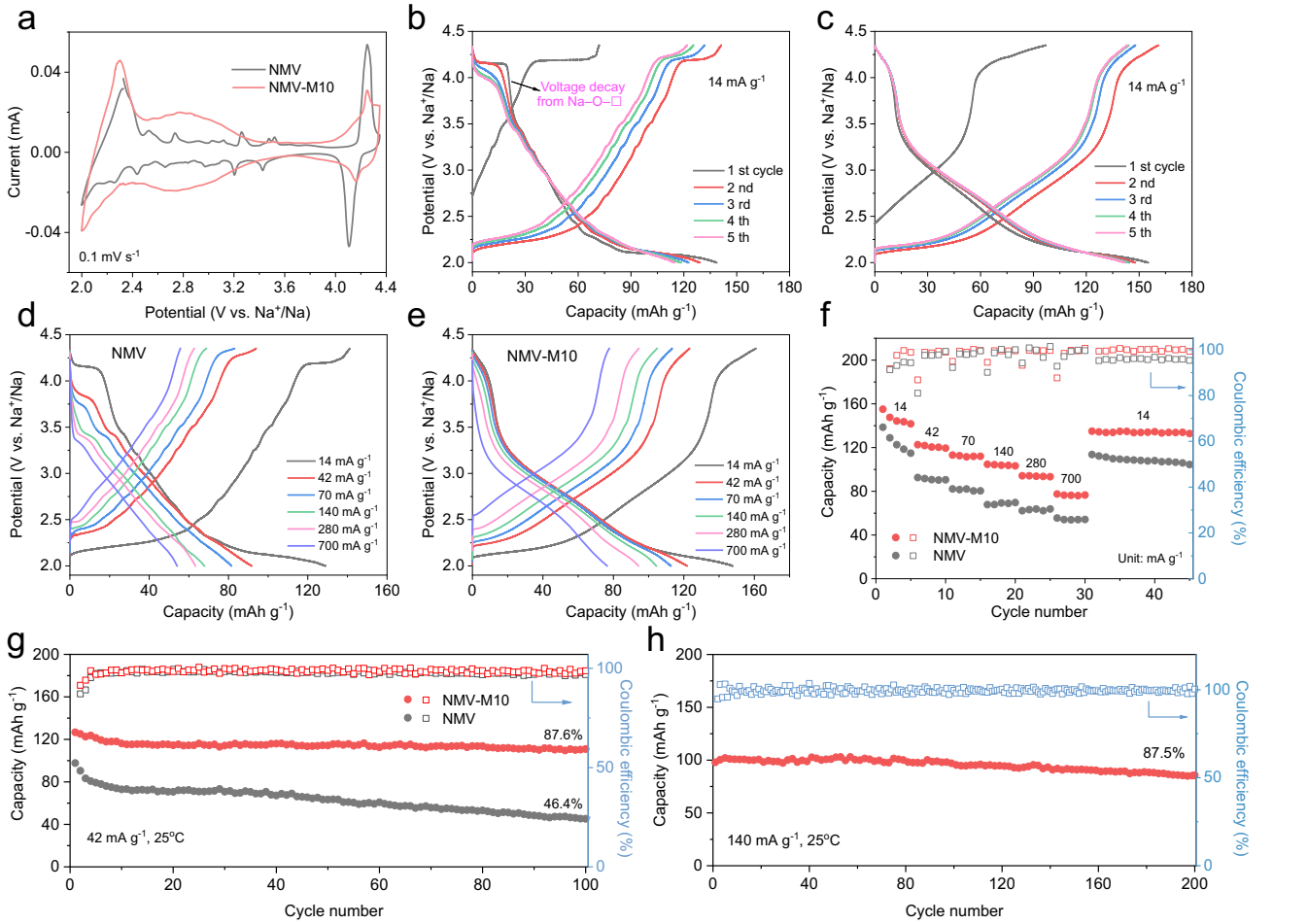

Fig. 2 | Electrochemical performances of NMV and NMV-M10 in 2.0–4.35 V (*vs.* Na^+/Na). **a** CV curves of NMV and NMV-M10 at 0.1 mV s^{-1}; GCD profiles of **b** NMV and **c** NMV-M10 at 14 mA g^{-1}; representative GCD profiles of **d** NMV and **e** NMV-M10 at different current densities; **f** rate performances and **g** cycling performances and Coulombic efficiencies of the NMV and NMV-M10 at 42 mA g^{-1}; **h** cycling performance of NMV-M10 at 140 mA g^{-1}. All the batteries are two-electrode coin cells, which were tested at 25 °C and the mass loading of active materials are in the range of 1–1.5 mg cm^{-2}.

cycles[37]. In comparison, the P2 structure has demonstrated higher intrinsic ionic conductance and suitable crystal symmetry, which may facilitate the reversibility of Na–O–□ here[38]. In addition, the NMV-M10 demonstrates the highest capacities at 2.4–4.0 V and 2.0–2.4 V, suggesting the optimized Mg and vacancy doping contents.

To further demonstrate the effect of Mg doping on anionic redox reaction induced by Na–O–□, cyclic tests are performed in the potential range of 2.4–4.35 V to exclude the influence of cationic redox (Mn^{3+}/Mn^{4+}). The first 30 discharge profiles of NMV, NMV-M5, and NMV-M10 at 42 mA g^{-1} are displayed in Supplementary Fig. 12. NMV-M10 exhibits a comparable anionic capacity with NMV, and its shorter discharge plateau above 4.0 V suggests the decrease of Na–O–□ anionic redox contribution. With the introduction of Mg, the voltage plateau decay is significantly suppressed and the NMV-M10 exhibits the most reversible anionic redox reaction in 100 cycles. The results unambiguously demonstrate that the introduction of Mg has a positive effect on the reversibility of anionic redox reaction induced by Na–O–□.

Figure 2d-f displays the typical GCD profiles at different current densities and the rate performances of NMV and NMV-M10. No matter at what rate, the NMV-M10 demonstrates a higher discharge capacity and lower polarization than the NMV and NMV-M5 (Supplementary Fig. 9c-d). In particular, with the increasing of current density, the voltage plateau above 4.0 V exhibits a progressive decay in NMV. To understand the enhanced rate capability of NMV-M10, galvanostatic intermittent titration technique (GITT, Supplementary Fig. 13) is employed. The NMV-M10 manifests a higher Na^+ diffusion coefficient (D_{Na^+}) than NMV, especially in the high voltage region, which is conducive to the rate performance.

The cycling performances at 2.0–4.35 V including both anionic and cationic redoxes are shown in Fig. 2g. The NMV-M10 delivers a high initial capacity of 126.7 mAh g^{-1} at 42 mA g^{-1} with a capacity retention of 87.6% over 100 cycles. At the same rate, the NMV (97.7 mAh g^{-1}, 46.4%) and NMV-M5 (107.4 mAh g^{-1}, 78.1%, Supplementary Fig. 9e) show much lower capacities and capacity retentions. Moreover, for NMV-M10, the average voltage shows negligible decrease over 100 cycles and the energy density retention reaches as high as 92.1%. In contrast, the average voltage of NMV decreases sharply and the retention of energy density is only 45.4% (Supplementary Fig. 14). For comparison, the NMM with only Mg (10%) doping was also synthesized with a pelleting process to shorten the diffusion distance in the particles at high-temperature sintering. The GCD profile of NMM at 14 mA g^{-1} doesn't show the plateau of the Na–O–□ configuration, suggesting the elimination of vacancies (Supplementary Fig. 15). The NMM exhibits a relatively low capacity of 117.8 mAh g^{-1} at 14 mA g^{-1} with a capacity rentention of 70.8% after 100 cycles at 42 mA g^{-1}. The better cyclic performance of NMM than NMV suggests that Mg doping has a positive effect on the cyclability. The cycling performance of NMV-M10 at

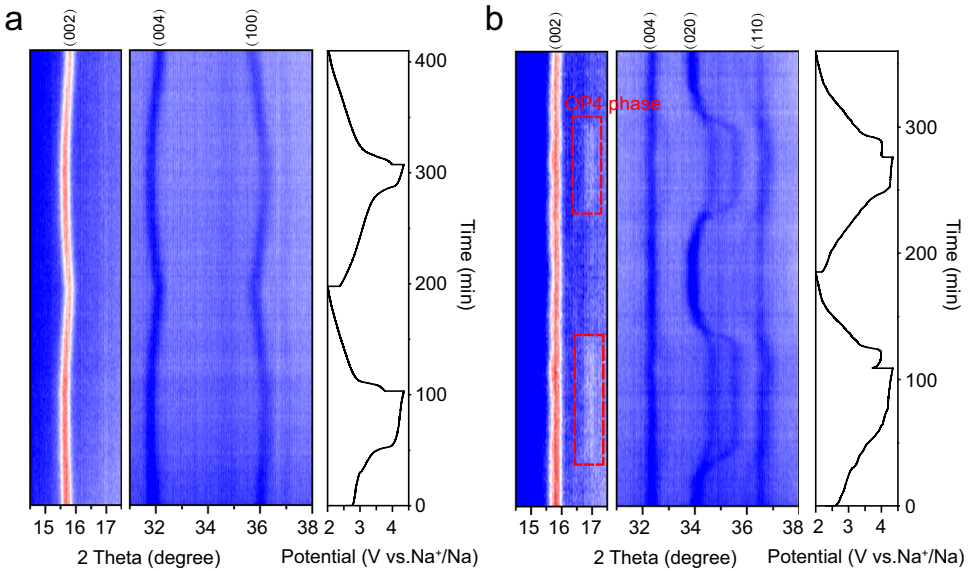

Fig. 3 | Structural evolutions of NMV and NMV-M10 during charge/discharge processes. In situ XRD patterns of **a** NMV-M10 and **b** NMV.

140 mA g^{-1} is shown in Fig. 2h. It manifests a capacity retention of 87.5% over 200 cycles, demonstrating its ideal cycling stability. From the above results, it can be concluded that the NMV-M10 manifests not only enhanced capacity and cyclability, but also suppressed voltage decay.

Full cells are assembled with NMV-M10 cathode and pre-sodiated hard carbon (HC) anode. The electrochemical performances of HC are presented in Supplementary Fig. 16. The first five GCD profiles and cycling performance of the full cells are presented in Supplementary Fig. 17. The GCD profiles generally overlap, except for the initial charge process. The full cell also delivers a good cyclability, with a capacity retention of 76% over 50 cycles, demonstrating the application potential of NMV-M10 in SIBs.

Structural evolution and charge compensation

Layered Na_xTMO_2 is usually susceptible to phase transformation in the high voltage region owing to the extraction of most Na^+. The structural evolution of NMV-M10 and NMV upon Na^+ extraction/insertion during the first two cycles are monitored by in situ XRD (Fig. 3 and Supplementary Fig. 18). For NMV-M10, the (002) and (004) diffractions shift towards lower angle during initial charging, while the (100) diffraction shifts towards higher angle. Such changes indicate the lattice expansion along the *c*-axis and lattice shrinkage along the *a*-axis. The expansion along *c*-axis during charging process is ascribed to the continous extraction of Na^+ from the TMO_2 interlayers, which reduces the shielding of positive charges and increases electrostatic repulsions between the oxygen layers, resulting in the increase of interlayer distance. While the shrinkage along *a*-axis is related to the oxidation of small amount of Mn^{3+} and oxygen. Upon discharging, the above-mentioned peaks shift back to their original positions, indicating the reversible structural evolution. No new peaks appear during the whole charge/discharge processes, indicating the P2 structure is well maintained. The variations in lattice parameters and cell volume during the first two cycles are presented in Supplementary Fig. 19. The maximum volume change is as low as 1.47%, demonstrating the near-zero-strain insertion/extraction characteristic of NMV-M10. When compared to other layered oxide cathode materials, the volume change of NMV-M10 is markedly small. For NMV, although the (002) and (004) peaks exhibit no obvious shifting, a new OP4 phase appears when the voltage reaches above 3.4 V, which is an intermediate phase of the transformation from P2 to O2 phase[39]. The appearance of OP4 phase suggests that the oxygen layer glides due to Na^+ extraction.

To further reveal the microstructure evolution of NMV-M10, in situ Raman, which is sensitive to the change of crystal and local structures[40], is conducted (Fig. 4a). The NMV-M10 presents three primary Raman peaks. The band at ~645 cm^{-1} is assigned to the symmetric stretching vibration (A_{1g}) of Mn−O bond in layered oxides. The bands at ~600 and ~488 cm^{-1} are assigned to the stretching vibrations of E_{2g} modes involving both Na and O vibrations, which are associated with the atomic displacements along the *c*-axis and *ab* plane, respectively[41–43]. The peak position of A_{1g} mode shows an insignificant shift during charging and discharging, indicating the robust Mn−O bonds. However, it broadens gradually at high voltage, which is related to the increased lattice distortion[44]. The band at ~600 cm^{-1} of the E_{2g} mode shows a red shift to ~580 cm^{-1} during charging over 3.4 V, which is attributed to the increase of interlayer distances due to Na^+ extraction. Notably, this peak still exists in fully charged state, which implies there is no transition from P2 to OP4 phase[41]. In addition, the blue shift of the peak at ~488 cm^{-1} during charge process is related to the shrinkage along *a* and *b* axes. All peaks return to the pristine positions during the subsequent discharge process, indicating the reversible structural evolution. From in situ XRD and Raman characterizations, one can know that when the voltage reaches above 3.4 V, the NMV-M10 just shows distortions in the MnO_6 octahedra, while the NMV presents a new OP4 phase. This suggests that the oxygen layers are fixed by the mis-occupied Mn ions in NMV-M10.

Atomic-scale HAADF-STEM is used to directly visualize the phase structure evolutions of NMV-M10 (Fig. 4b) and NMV (Fig. 4c). For the NMV-M10 charged to 4.35 V, there are still many bright contrasts existing in the Na layers, corresponding to the mis-occupied Mn ions. The still presence of the mis-occupied Mn ions when most of Na^+ are extracted confirms the robust pinning effect. In addition, the TM columns are well aligned with no layer gliding (indicated by the yellow line), which is consistent with the pristine P2 structure. In contrast, the HADDF-STEM image of NMV charged to 4.35 V shows that some adjacent layers are offset from one another (indicated by green lines). The layer gliding implies the existence of OP4 phase, in agreement with the in situ XRD results. From the above discussions, it can be concluded that the mis-occupied Mn ions can act as “rivets” to fix the oxygen layers when Na^+ ions are extracted at the high voltage region, thus improving the structural stability.

To further investigate the anionic redox behavior, ex situ XPS is performed to characterize the electronic structure of oxygen at various charge/discharge states. The ex situ O 1*s* XPS spectra of NMV-M10

https://doi.org/10.1038/s41467-024-54998-1

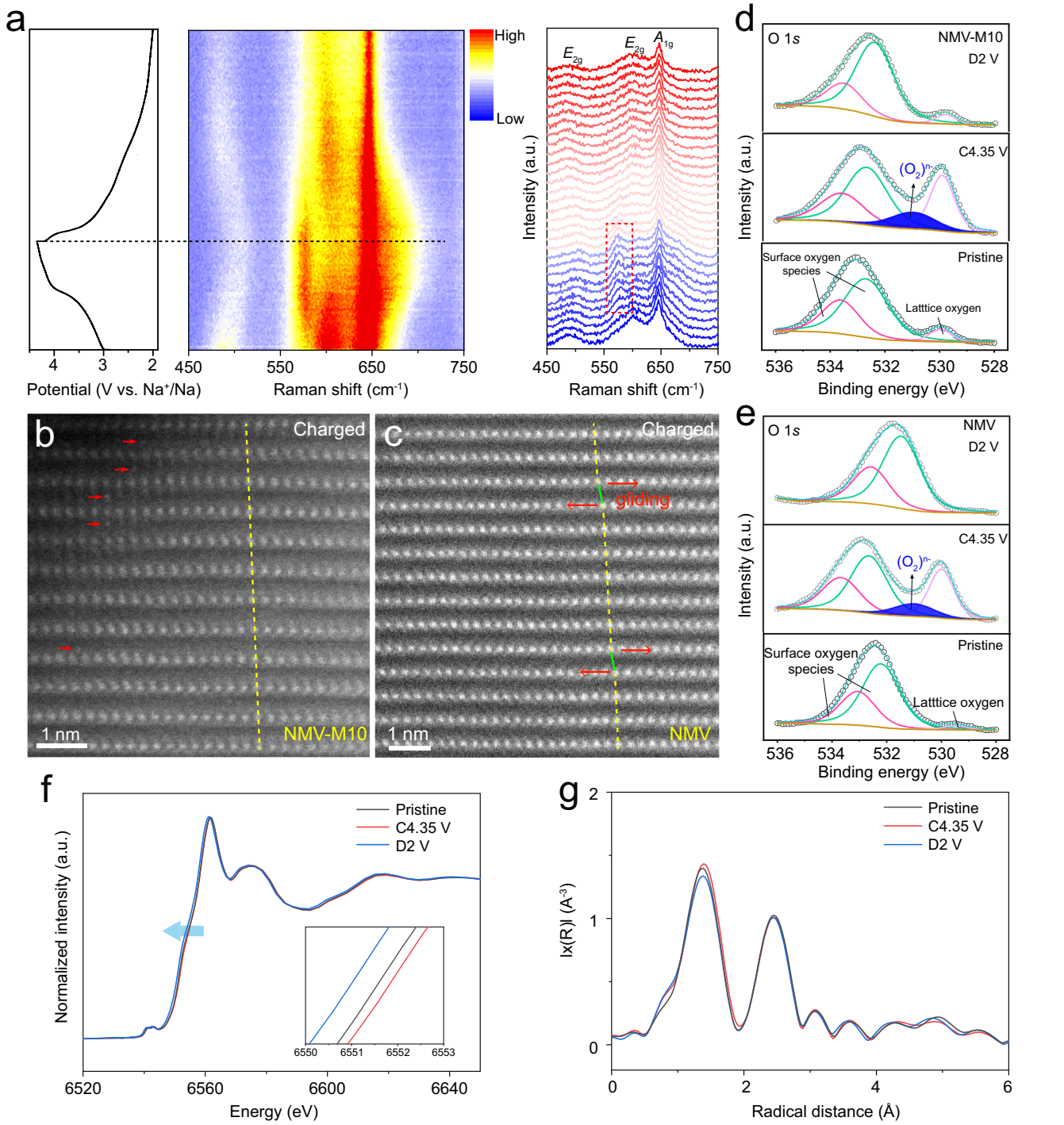

Fig. 4 | Microstructure evolution and charge compensation mechanism in NMV-M10. a In situ Raman spectra of NMV-M10, the band of the E_{2g} mode shows a red shift (marked by red rectangle) during charging over 3.4 V; atomic-scale HAADF-STEM images of **b** NMV-M10 (riveted Mn ions are marked with red arrows) and **c** NMV; ex situ O 1*s* XPS spectra of **d** NMV-M10 and **e** NMV; ex situ Mn *K*-edge **f** XANES and **g** EXAFS spectra of NMV-M10.

and NMV are provided in Fig. 4d, e. For both NMV-M10 and NMV, the pristine O 1*s* spectra can be divided into two peaks from the surface oxygen-related species and one peak from lattice oxygen. After charging to 4.35 V, an extra component at 531.0 eV appears, which can be ascribed to the formation of peroxo-like $(O_2)^{n-}$ species[45]. This phenomenon evidences that the oxygen redox activity has been triggered to participate in the charge compensation process in both NMV-M10 and NMV.

Ex situ Electron Energy loss spectroscopy (EELS) has been performed to further demonstrate the oxygen redox in NMV-M10, which gives insight into the electronic structure changes of O-K and Mn-L edge peaks in the material upon cycling. The EELS spectra are collected by linear scanning from surface to bulk (Supplementary Fig. 20). As displayed in the bulk (Supplementary Fig. 20g), the pre-edge around 535 eV in the O EELS K-edge spectrum is related to the transition of O 1*s* electrons to the unoccupied 2*p* orbitals, which is hybridized with the TM 3*d* orbitals. When charging to 4.35 V, the increase of pre-edge intensity indicates the removal of electrons from oxygen, namely the increase of oxygen holes, which is contributed by the oxygen redox[46–48]. After discharging to 2.0 V,

the intensty decreased, suggesting the good reversibility of oxygen redox.

To analyze the electronic structure and redox behavior of oxygen in transition metal oxides, O *K*-edge soft X-ray absorption spectroscopy (sXAS) and mapping resonant inelastic X-ray scattering (mRIXS) are both the common approach to being employed[23,49]. sXAS can effectively identify oxygen redox activity by detecting changes in the pre-edge features and the intensity of the main absorption peaks. These changes are associated with the formation of electron holes on oxygen during the redox process. mRIXS is particularly sensitive to short-range order and can distinguish between different oxygen species, such as molecular O_2, O_2^{2-} and O^{2-}[50,51]. While mRIXS can distinguish between various oxidized states of oxygen, and gives a comprehensive picture of the electronic structure by mapping the energy loss features associated with specific electronic transitions, sXAS is relatively straightforward and widely available, making it a common choice for initial investigations of oxygen redox activity. Herein, the ex-situ sXAS at different charged states are performed. As shown in Supplementary Fig. 21, the sXAS spectra at O *K*-edges were collected using the total fluorescence yield (TFY) mode. The dominant pre-edge peaks below 533 eV correspond to the transition of O 1*s* electrons to the unoccupied 2*p* orbitals, which is hybridized with TM 3*d* orbitals. The intensity change of the pre-edge peak area during charge/discharge reflects the covalent intensity of TM 3*d* and O 2*p* or the generation of electron holes on oxygen[31]. With the charging of NMV-M10 from pristine state to 4.35 V, the obvious increase in the O *K*-edge pre-edge area can be observed, which implies the removal of electrons from oxygen and an increase in the electron holes on oxygen, meanwhile, the shoulder position at 530.5 eV gets elevated, suggesting the participation of oxygen redox.

Ex situ X-ray absorption near-edge spectroscopy (XANES) measurements are performed to investigate the valence state change in NMV-M10 (Fig. 4f). After charging to 4.35 V, the Mn *K*-edge XANES spectra slightly shift towards higher energy, suggesting the oxidation of partial Mn^{3+} for charge compensation. When discharging to 2.0 V, the enlarged Mn *K*-edge XANES shows a shift to lower energy, indicating the reduction of Mn^{4+} to Mn^{3+} state. The extended X-ray absorption fine structure (EXAFS) spectra are employed to show coordination environment of Mn. Two dominant peaks can be observed in the Fourier transformation of EXAFS (Fig. 4g), which correspond to Mn–O bond and Mn–M_e interaction. The Mn–O distance shows a slightly increase during charge process, possibly due to the oxygen redox reaction that weakens the Mn-O bond. Upon discharging to 2.0 V, the Mn–O distance shows a slight decrease. The negligible change of Mn–M_e distance during charge/discharge implies the stable structure of NMV-M10. The ex situ Mn XPS spectra of NMV and NMV-M10 in Supplementary Fig. 22 demonstrate similar changes. With charging from pristine state to 4.35 V, small amounts of Mn^{3+} are oxidized to Mn^{4+}. After discharging to 3.5 V, Mn $2p_{3/2}$ peak becomes slightly broadened, which indicates that a very small amounts of Mn^{4+} are reduced to Mn^{3+} and the capacity contribution in this voltage range is mainly provided by anionic (oxygen) redox. When further discharged to 2 V, a large amount of Mn^{4+} are reduced and the electrochemical oxidation center changes from anionic redox to cationic redox of Mn^{3+}/Mn^{4+}. Therefore, it can be concluded that most of the Mn^{3+}/Mn^{4+} redox are proceeded at lower than 3.5 V, and a very small amounts proceed above 3.5 V.

Origin of the cracks

In situ XRD already demonstrate that the NMV-M10 possesses a more stable layered structure than NMV during the first two cycles. To further probe the stability after repeated cycles, ex situ XRD patterns of NMV-M10 and NMV are collected at different cycles, and the electrodes are cycled at 42 mA g^{-1} within 2.0–4.35 V. The P2 structure of NMV-M10 can be well maintained when charged to 4.35 V at the 1st, 20th, 60th, and 100th cycles (Fig. 5a). No residue peaks can be observed, indicating that the P2 to O2 phase transformation has been well inhibited. The SEM image (Fig. 5a inset) after 100 cycles shows that the NMV-M10 particles remain intact without obvious cracks, indicating the good structural stability. In contrast, for NMV, the diffraction peaks from OP4 and O2 phases strengthen progressively after cycling (Fig. 5b). Such phase transitions from P-type to O-type phases are generally accompanied by a large volume change, which is usually detrimental to the structural stability[52]. After 100 cycles, the particles show a shale-like structure (Fig. 5b inset and Supplementary Fig. 23) with stacked flakes, which is the result of layer gliding and crack accumulation. The structural deterioration should be responsible for the severe capacity decay of NMV.

HAADF-STEM is used to further probe the origin of the cracks in NMV. An atomic-scale HAADF-STEM image of the NMV at charged state (4.35 V) is displayed in Fig. 5c. Clear TM layers with obvious distortions can be observed at both sides of the crack. The interlayer distance close to the crack is smaller than that in the bulk, indicating the evolution from P-type to O-type phase preferentially takes place at the edge of crack. Such cracks might be occurred due to the irreversible layer gliding induced delamination. The EDS elemental mappings show that the O and Mn elements are homogeneously distributed in the particle, while some obvious Na-deficient regions can be observed (Fig. 5d). The Na-deficient regions are generally distributed around the cracks, which suggests that the excessive extraction of Na^+ causes the oxygen layer gliding and crack formation due to the accumulated electrostatic repulsion. The relative atomic fractions determined from different areas around the crack confirms the above conclusion (Supplementary Fig. 24). From the above discussions, it can be concluded that the mis-occupied Mn ions induced by Mg doping in NMV-M10 act as “rivets” and are sufficiently robust to suppress the layer gliding and thus inhibit the crack formation. As a result, the NMV-M10 demonstrates not only increased anion redox capacity, but also improved structural stability (Fig. 5e).

Theoretical calculations

As discussed above, the NMV-M10 with dual Mg and vacancy doping features improved oxygen redox activity and reversibility than the individual vacancy and Mg doping, which may suggest the dual Mg and vacancy doping is beneficial for placing the nonbonding O 2*p* band close to the E_f. Therefore, the electronic structures are calculated by DFT calculations to study the effects of Mg and vacancy doping on O 2*p* and Mn 3*d* bands. The crystal models of $Na_8Mn_{12}O_{24}$ (NM), $Na_8Mn_{11}O_{24}$ (NMV), $Na_8Mn_{11}MgO_{24}$ (NMM) and $Na_8Mn_{10}MgO_{24}$ (NMV-M) are shown in Supplementary Fig. 25. The projected density of states (pDOS) of Mn 3*d* and O 2*p* states are presented in Fig. 6a and Supplementary Fig. 26. For the pristine NM, the Mn^{3+}-e_g states dominate the vicinity of E_f, indicating the charge compensation during the initial charging is realized through the Mn^{3+}/Mn^{4+} redox[53], and the O 2*p* state is quite below E_f. When vacancies (~8%) are introduced (NMV), the O 2*p* state gets close to the E_f. The NMM with only Mg doping also exhibits an elevated O 2*p* band towards E_f, suggesting the anionic redox activity of Na-O-Mg (Supplementary Fig. 26). For NMV-M, the existence of both Mg^{2+} and vacancies make the O 2*p* state further approach to the E_f, suggesting the oxygen redox will participate in the charge compensation during charging. In addition, the reduction of Mn^{3+}-e_g states implies the decrease of Mn^{3+} contents induced by Mg doping. The partial charge density distributions of NM and NMV are calculated to reveal the local status of electrons (Fig. 6b-c). With the introduction of vacancies, the electron cloud of the contiguous O exhibits no overlapping, implying the existence of nonbonding O 2*p* orbitals, which is responsible for the oxygen redox reaction. The crystal orbital Hamilton populations (COHP) analysis was performed to investigate the chemical bonding

https://doi.org/10.1038/s41467-024-54998-1

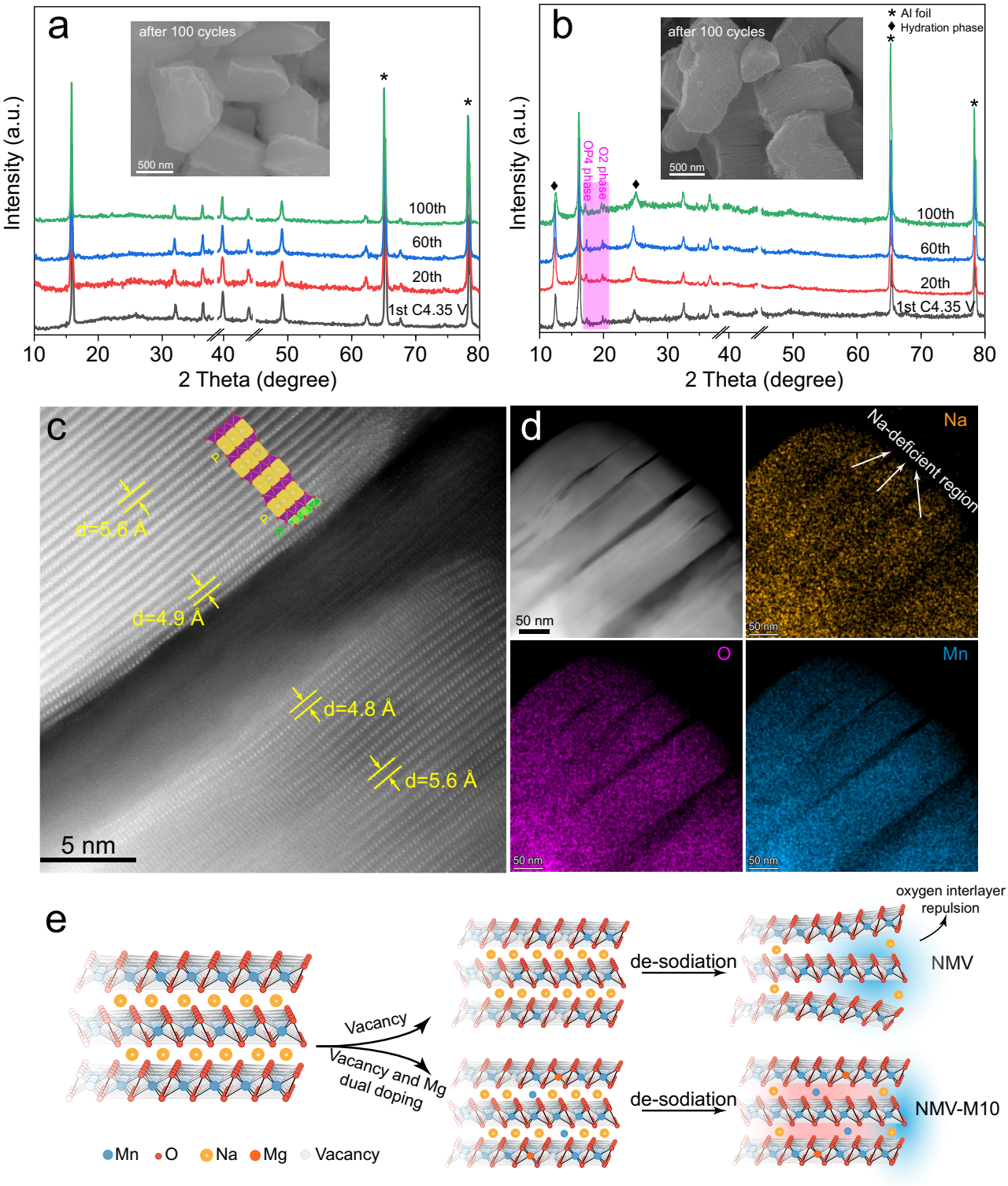

Fig. 5 | Structural deterioration mechanism in NMV. Ex situ XRD patterns of **a** NMV-M10 and **b** NMV, the insets are the SEM images after 100 cycles, the OP4 and O2 phases are highlighted in (**b**); **c** atomic-scale HAADF-STEM image of the NMV at the first charged state; **d** HAADF-STEM image of the NMV at the first charged state and the corresponding EDS mappings; **e** schematic illustration of the structural evolution of NMV-M10 and NMV.

information (Fig. 6d). Especially, the integrated COHP (ICOHP) was calculated to reflect the bonding strength of the Mn–O bond adjacent to the vacancy. The larger ICOHP value of Mn–O after Mg doping indicates its stronger bond strength, which would suppress TM migration in the TMO_2 layer, thus preventing the formation of vacancy clusters. As revealed by Robert A. House et al.[54], the formation of O_2 molecules inside the crystal is only possible due to TM migration that creates vacancy clusters. These clusters serve as sites for trapping O_2 molecules generated during charging, leading to voltage hysteresis and irreversibility of the oxygen redox process in the first cycle. Combing the results of XPS and sXAS, the oxygen redox products of NMV-M10 are mainly $(O_2)^{n-}$ species instead of O_2

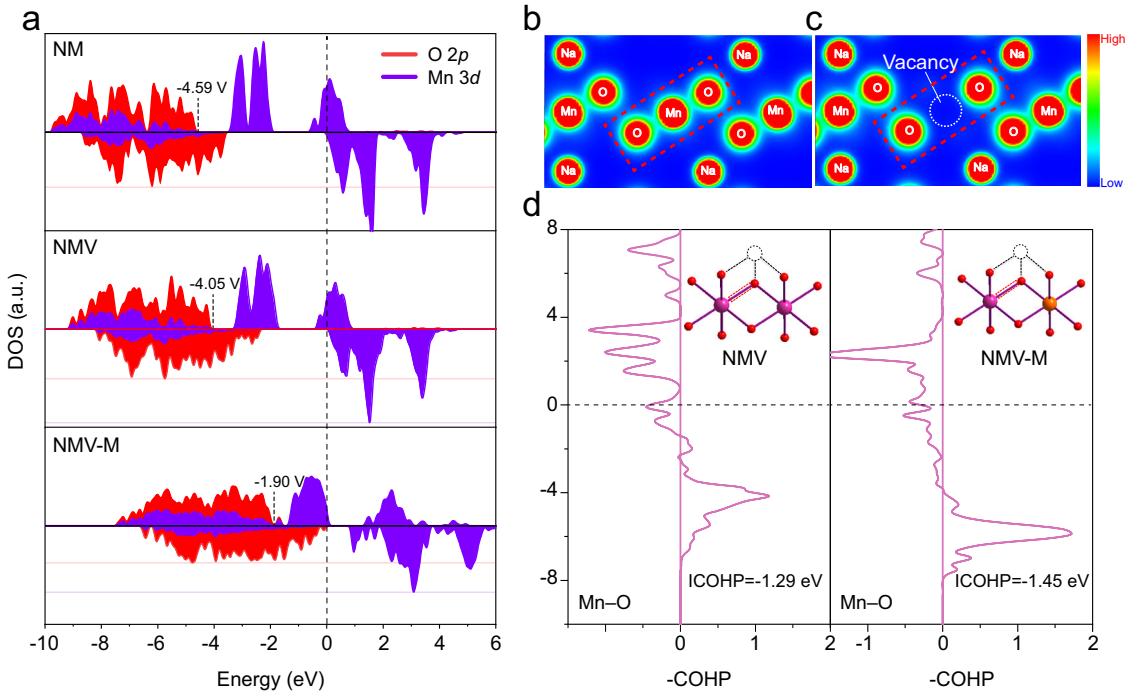

Fig. 6 | DFT calculations about the electronic structure with Mg and vacancy doping. a The calculated pDOS of NM, NMV, and NMV-M; The partial charge density of **b** NM and **c** NMV; **d** COHP calculations of the Mn–O bond in NMV and NMV-M.

molecules, which inversely proves that the irreversible formation of molecular O_2 is suppressed. This suggests that Mg doping strengthens the Mn-O bond, inhibiting Mn migration and preventing the formation of vacancy clusters. This stabilization mechanism effectively enhances electrochemical performance by promoting high anionic reversibility.

Discussions

In summary, a strategy for Mg ion and vacancy dual doping with partial TM ions pinned in the Na layers has been developed to simultaneously improve the oxygen redox reversibility and structural stability of layered oxides. Both the Mg ions and vacancies are contained in the TM layers and partial Mn ions occupy the Na-sites. DFT calculations demonstrate that the doped Mg ions combined with native vacancies can create abundant nonbonding O *2p* orbitals along the Na–O–Mg, Na–O–□, and Mg–O–□ configurations, which make the O 2*p* band closer to the E_f and significantly contribute to the capacity derived from oxygen redox. The introduction of Mg also suppresses the voltage decay of Na–O–□ due to the strengthened Mn–O bond. Advanced in situ and ex situ characterizations reveal that the mis-occupied Mn ions in the Na layers function as "rivets" to suppress the slab gliding at deep de-sodiated state and thereby inhibit the generation of cracks. Consequently, the obtained P2-type $Na_{0.67}Mn_{0.011}[Mg_{0.1}□_{0.07}Mn_{0.83}]O_2$ demonstrates significantly improved capacity (155.1 mAh g^{-1} at 14 mA g^{-1}) and cyclability (87.5% capacity retention after 200 cycles at 140 mA g^{-1}) over the un-doped sample. This study provides an effective strategy to improve the anionic redox reversibility and structural stability of layered oxides for high energy-density and stable sodium storage.

Methods

Chemicals

Oxalic acid (99.7%), sodium nitrate ($NaNO_3$, 99.7%), magnesium nitrate hexahydrate ($Mg(NO_3)_2{\cdot}6H_2O$, 99.7%), and manganese acetate tetrahydrate ($Mn(CH_3COO)_2{\cdot}4H_2O$, 99.7%) were purchased from Sinopharm Chemical Reagent Co., Ltd. (Shanghai, China). All the chemicals were used without further purification. Deionized water (18.2 MΩ·cm) was used throughout the experiment.

Materials preparation

The $Na_{0.67}Mn_{0.011}[Mg_{0.1}□_{0.07}Mn_{0.83}]O_2$ compound was synthesized by a simple organic acid-assisted solid state reaction method. Firstly, oxalic acid (44 mmol) was dissolved in 20 mL deionized water and stirred vigorously for 2 h. Then, $NaNO_3$ (6.7 mmol, 5 wt.% in excess according to stoichiometry), $Mg(NO_3)_2{\cdot}6H_2O$ (1 mmol), $Mn(CH_3COO)_2{\cdot}4H_2O$ (9 mmol, 99%) were added stepwise and stirred for 2 h. The suspension was heated to 80 °C overnight to evaporate the water and further dried at 180 °C for 3 h. The as-obtained powder was ground manually and then heated to 500 °C for 2 h and 800 °C for 10 h in air at 2 °C min^{-1}. Then, the sample was cooled down to 500 °C at 1 °C min^{-1} and naturally to room temperature, and stored in an Ar-filled glovebox. The synthesis conditions for control samples can be found in Supplementary Table 4. The synthesis process of NMM is similar to NMV-M10 except adding a pelleting process (pressure is 20 MPa) before sintering at 800 °C for 10 h.

Material characterization

X-ray diffraction (XRD) was performed on a Bruker D8 Advance X-ray diffractometer with a Cu Kα X-ray source (λ = 1.5406 Å). Scanning electron microscopy (SEM) were performed on a JEOL-7100F microscope at 20 kV. High-angle annular dark-field (HAADF) and annular bright field (ABF)—scanning transmission electron microscopy (STEM) images and atomic-scale STEM X-ray energy dispersive spectroscopy (EDS) mappings were conducted on Titans Themis. Chemical composition of the samples was determined by inductively coupled plasma-optical emission spectrometer (ICP-OES, SPECTRO-BLUE). Raman spectra were recorded using a Horiba LabRAM HR Evolution with a 532 nm excitation laser, before testing, the device was calibrated to the standard position with a Si sheet. X-ray photoelectron spectroscopy (XPS) was carried out on a Thermo-Fisher Scientific-ESCALAB 250Xi equipped with an Al Kα monochromated X-ray source, which was calibrated with gold and silver samples before the testing. X-ray

absorption spectroscopy (XAS) measurements were collected at 12-BM-B at the Advanced Photon Source (APS) in Argonne National Laboratory. The radiation was monochromatized by a Si (111) double-crystal monochromator. To reduce the uncertainty of the measurements, for each characterization, all samples were tested on the same device and the device was calibrated with a reference sample.

Statistics and reproducibility

No data were excluded from the analyzes. No statistical method was used to predetermine sample size. All synthesis and electrochemical experiments were performed at least three times independently, ensuring the reproducibility of the results.

Electrochemical characterization

The electrochemical performances were tested by assembling CR2016 coin cells in the Ar-filled glove box, which is consisted of positive and negative stainless steel shells, a piece of single-coated cathode electrode, sodium foil, separator, electrolyte, and two pieces of round stainless steel mesh (15 mm × 0.15 mm, 50 mesh). Sodium foil (Aladdin, 99.7%) was used as both the counter and reference electrodes, the sodium foil was prepared by rolling the bulk sodium metal to a thickness of ~1 mm in an Ar-filled glove box and punching into a disc with a diameter of 14 mm. 70 wt.% of active materials, 20 wt.% of acetylene black (99.9% purity, Guangdong Canrd New Energy Technology Co.) were hand-ground in a mortar for 20 mins, then transferred into a vial and 10 wt.% of polyvinylidene fluoride (99.5%, Guangdong Canrd New Energy Technology Co.) in N-methyl-2-pyrrolidone (Aladdin, 99.9%) was added and stirred for 4 h. After homogeneous mixing, the obtained slurry was single-side coated onto Al foil and dried at 100 °C in a vacuum oven overnight, after which it was punched into 10 mm discs as the working electrodes. 1.0 M $NaPF_6$ in propylene carbonate (PC) containing 5% of fluoroethylene carbonate (FEC) was used as the electrolyte and glass fiber (Whatman, GF/D) with a diameter of 16 mm was used as the separator, on which 150 µL of electrolyte was added to ensure the wetting. The mass loading of active materials was 1–1.5 mg cm^{-2}. GCD measurements were performed on a NEWARE battery testing system within the potential range of 2.0–4.35 V (*vs.* Na^+/Na). CV tests were conducted on CHI600E electrochemical workstations. All the electrochemical tests were performed in a room with a controllable temperature of 25 °C.

Full-cell assembly. The positive and negative electrodes were composed of 70 wt.% of NMV-M10 or hard carbon (HC), which was purchased from BTR New Material Group Co., Ltd (Shenzhen, China), 20 wt.% of acetylene black and 10 wt.% of polyvinylidene fluoride. Both the electrodes were punched into discs with the same diameter of 10 mm. The mass loading of the positive and negative electrodes in the full cells were around 1.2–1.5 and 0.9–1.2 mg cm^{-2}, respectively. 1.0 M $NaPF_6$ in PC:EC (1:1, v:v) containing 5% of FEC was used as the electrolyte and GF/D glass fiber with a diameter of 16 mm was used as the separator, on which 200 µL of electrolyte was added to ensure the wetting of electrodes. The electrochemical performances of the full cell were evaluated in CR2016 coin cells. Berfore assemblying the full cells, the HC electrode was pre-sodiated by assemblying the half cell with sodium metal, 1.0 M $NaPF_6$ in PC:EC (1:1, v:v) containing 5% of FEC and GF/D glass fiber were used as the electrolyte and separator. The HC electrode was discharging and charging for 5 cycles within 0.01–2.0 V to form stable SEI film. And the cell was disassembled in the glove box when the discharge volatge is 0.1 V. Then the HC||NMV-M10 full cell was assembled with the obtained pre-sodiated HC anode and NMV-M10 cathode. The full cells were tested without additional formation cycle.

In-situ and ex-situ characterization. For in situ XRD and Raman tests, the tested devices are schematically illustrated in Supplementary Fig. 27. The electrodes were prepared by mixing 80 wt.% of active materials, 10 wt.% acetylene black and 10 wt.% of polytetrafluoroethylene. 1.0 M $NaPF_6$ in PC containing 5% of FEC and GF/D glass fiber with a diameter of 16 mm were used as the electrolyte and separator, respectively, on which 200 µL of electrolyte was added. The electrode was cut into 8 × 8 mm squares and the mass loading of active materials was 1–1.5 mg cm^{-2}. The sodium metal was punched to a diameter of 14 mm and a thinckness of ~1 mm. The current density of the in situ tests are 50 mA g^{-1}. For ex situ measurements, the electrodes were disassembled from the coin cell in an Ar-filled glove box (H_2O < 0.1ppm; O_2 < 0.1ppm), then washed with the dimethyl carbonate (DMC, Aladdin, 99.9%) solution repeatedly, and dried in the glove box.

Theoretical calculations

The Vienna Ab-Initio Package (VASP) was employed to perform density functional theory (DFT) calculations within the generalized gradient approximation (GGA) using the Perdew, Burke, and Enzerhof (PBE) formulation[55,56]. The projected augmented wave (PAW) potentials were applied to describe the ionic cores and take valence electrons into account using a plane wave basis set with a kinetic energy cutoff of 450 eV. Partial occupancies of the Kohn–Sham orbitals were allowed using the Gaussian smearing method and a width of 0.05 eV. The electronic energy was considered self-consistent when the energy change was smaller than 10^{-4} eV. A geometry optimization was considered convergent when the force change was smaller than 0.03 eV/Å. Grimme's DFT-D3 methodology was used to describe the dispersion interactions. The equilibrium lattice constants of structures were optimized using a 3×3×2 Monkhorst-Pack k-point grid for Brillouin zone sampling. The U correction had been used for Mn atoms, and it had been set at 4.21 eV. The bonding properties of Mn–O were disclosed by the COHP analysis[57,58], as implemented in the LOBSTER code[59]. The equilibrium lattice constants of $NaMnO_2$ unit cell were optimized. These optimized constants were then used to construct a 2×2×2 supercell model. The $Na_8Mn_{11}O_{24}$ or $Na_8Mn_{11}MgO_{24}$ structures were established with randomly deleting a Mn atom as a vacancy or doping Mg at the Mn position, given the symmetric nature of the Mn-O system. $Na_8Mn_{10}MgO_{24}$ structures were established by doping Mg at the Mn position and Mn in Na position in $Na_8Mn_{11}O_{24}$ structures.

Data availability

The data supporting the plots in this paper and its Supplementary Information are available. All other relevant data that support the findings of this study can be obtained from the corresponding authors upon request. Source data are provided with this paper.

References

1. Yabuuchi, N., Kubota, K., Dahbi, M. & Komaba, S. Research Development on Sodium-Ion Batteries. *Chem. Rev.* **114**, 11636–11682 (2014).
2. Zhao, C. et al. Rational Design of Layered Oxide Materials for Sodium-Ion Batteries. *Science* **370**, 708–711 (2020).
3. Chen, S. et al. Challenges and Perspectives for NASICON-Type Electrode Materials for Advanced Sodium-Ion Batteries. *Adv. Mater.* **29**, 1700431 (2017).
4. Hwang, J., Myung, S. & Sun, Y. Sodium-Ion Batteries: Present and Future. *Chem. Soc. Rev.* **46**, 3529–3614 (2017).
5. Cai, C. et al. Encapsulation of $Na_4MnV(PO_4)_3$ in Robust Dual-Carbon Framework Rendering High-energy, Durable Sodium Storage. *J. Phys. Energy* **2**, 025003 (2020).
6. Wang, M. et al. The Prospect and Challenges of Sodium-Ion Batteries for Low-Temperature Conditions. *Interdiscip. Mater.* **1**, 373–395 (2022).
7. Park, Y. J. et al. A New Strategy to Build a High-Performance P'2-Type Cathode Material through Titanium Doping for Sodium-Ion Batteries. *Adv. Funct. Mater.* **29**, 1901912 (2019).

8. Yuan, T. et al. A High-Rate, Durable Cathode for Sodium-Ion Batteries: Sb-Doped O3-Type Ni/Mn-Based Layered Oxides. *ACS Nano* **16**, 18058–18070 (2022).
9. Wang, Q. et al. Tuning P2-Structured Cathode Material by Na-Site Mg Substitution for Na-Ion Batteries. *J. Am. Chem. Soc.* **141**, 840–848 (2019).
10. Liu, Q. et al. Sodium Transition Metal Oxides: The Preferred Cathode Choice for Future Sodium-Ion Batteries? *Energy Environ. Sci.* **14**, 158–179 (2021).
11. Clément, R. J. et al. Structurally Stable Mg-doped P2-$Na_{2/3}Mn_{1-y}Mg_yO_2$ Sodium-Ion Battery Cathodes with High Rate Performance: Insights from Electrochemical, NMR and Diffraction Studies. *Energy Environ. Sci.* **9**, 3240–3251 (2016).
12. House, R. et al. Superstructure Control of First-Cycle Voltage Hysteresis in Oxygen-Redox Cathodes. *Nature* **577**, 502–508 (2020).
13. Guo, Y. et al. Boron-Doped Sodium Layered Oxide for Reversible Oxygen Redox Reaction in Na-ion Battery Cathodes. *Nat. Commun.* **12**, 5267 (2021).
14. Li, X. et al. Whole-Voltage-Range Oxygen Redox in P2-Layered Cathode Materials for Sodium-Ion Batteries. *Adv. Mater.* **33**, 2008194 (2021).
15. Rong, X. et al. Structure-Induced Reversible Anionic Redox Activity in Na Layered Oxide Cathode. *Joule* **2**, 125–140 (2018).
16. Seo, D.-H. et al. The Structural and Chemical Origin of the Oxygen Redox Activity in Layered and Cation-Disordered Li-Excess Cathode Materials. *Nat. Chem.* **8**, 692–697 (2016).
17. Li, B. & Xia, D. Anionic Redox in Rechargeable Lithium Batteries. *Adv. Mater.* **29**, 1701054 (2017).
18. Luo, K. et al. Charge-Compensation in 3*d*-Transition-Metal-Oxide Intercalation Cathodes Through the Generation of Localized Electron Holes on Oxygen. *Nat. Chem.* **8**, 684–691 (2016).
19. Clément, R. J., Lun, Z. & Ceder, G. Cation-Disordered Rocksalt Transition Metal Oxides and Oxyfluorides for High Energy Lithium-Ion Cathodes. *Energy Environ. Sci.* **13**, 345–373 (2020).
20. Du, K. et al. Exploring Reversible Oxidation of Oxygen in a Manganese Oxide. *Energy Environ. Sci.* **9**, 2575–2577 (2016).
21. Rong, X. et al. Anionic Redox Reaction-Induced High-Capacity and Low-Strain Cathode with Suppressed Phase Transition. *Joule* **3**, 503–517 (2019).
22. Maitra, U. et al. Oxygen Redox Chemistry without Excess Alkali-Metal Ions in $Na_{2/3}[Mg_{0.28}Mn_{0.72}]O_2$. *Nat. Chem.* **10**, 288–295 (2018).
23. Dai, K. et al. High Reversibility of Lattice Oxygen Redox Quantified by Direct Bulk Probes of Both Anionic and Cationic Redox Reactions. *Joule* **3**, 518–541 (2019).
24. Konarov, A. et al. Exceptionally Highly Stable Cycling Performance and Facile Oxygen-Redox of Manganese-based Cathode Materials for Rechargeable Sodium Batteries. *Nano Energy* **59**, 197–206 (2019).
25. Bai, X. et al. Anionic Redox Activity in a Newly Zn-Doped Sodium Layered Oxide P2-$Na_{2/3}Mn_{1-y}Zn_yO_2$ (0 <y<0.23). *Adv. Energy Mater.* **8**, 1802379 (2018).
26. Song, B. et al. Understanding the Low-Voltage Hysteresis of Anionic Redox in $Na_2Mn_3O_7$. *Chem. Mater.* **31**, 3756–3765 (2019).
27. Li, Y. et al. Native Vacancy Enhanced Oxygen Redox Reversibility and Structural Robustness. *Adv. Energy Mater.* **9**, 1803087 (2018).
28. Mortemard de Boisse, B. et al. A. Highly Reversible Oxygen-Redox Chemistry at 4.1 V in $Na_{4/7-x}[\square_{1/7}Mn_{6/7}]O_2$ (□: Mn Vacancy). *Adv. Energy Mater.* **8**, 1800409 (2018).
29. Zhao, C. et al. Decreasing Transition Metal Triggered Oxygen Redox Activity in Na-Deficient Oxides. *Energy Storage Mater* **20**, 395–400 (2019).
30. Kumakura, S., Tahara, Y., Kubota, K., Chihara, K. & Komaba, S. Sodium and Manganese Stoichiometry of P2-Type $Na_{2/3}MnO_2$. *Angew. Chem. Int. Ed.* **55**, 12760–12763 (2016).
31. Huang, Y. et al. Enabling Anionic Redox Stability of P2-$Na_{5/6}Li_{1/4}Mn_{3/4}O_2$ by Mg Substitution. *Adv. Mater.* **34**, 2105404 (2022).
32. Chu, S. et al. Pinning Effect Enhanced Structural Stability toward a Zero-Strain Layered Cathode for Sodium-Ion Batteries. *Angew. Chem. Int. Ed.* **60**, 13366–13371 (2021).
33. Liu, X. et al. P2-$Na_{0.67}Al_xMn_{1-x}O_2$: Cost-Effective, Stable and High-Rate Sodium Electrodes by Suppressing Phase Transitions and Enhancing Sodium Cation Mobility. *Angew. Chem. Int. Ed.* **58**, 18086–18095 (2019).
34. Clément, R. J., Bruce, P. G. & Grey, C. P. Review-Manganese-Based P2-Type Transition Metal Oxides as Sodium-Ion Battery Cathode Materials. *J. Electrochem. Soc.* **162**, A2589–A2604 (2015).
35. Wang, P. et al. Na^+/Vacancy Disordering Promises High-Rate Na-Ion Batteries. *Sci. Adv.* **4**, eaar6018 (2018).
36. Song, B. et al. A Novel P3-type $Na_{2/3}Mg_{1/3}Mn_{2/3}O_2$ as High Capacity Sodium-Ion Cathode Using Reversible Oxygen Redox. *J. Mater. Chem. A* **7**, 1491–1498 (2019).
37. Kim, E. J. et al. Vacancy-Enhanced Oxygen Redox Reversibility in P3-Type Magnesium-Doped Sodium Manganese Oxide $Na_{0.67}Mg_{0.2}Mn_{0.8}O_2$. *ACS Appl. Energy Mater.* **3**, 10423–10434 (2020).
38. Yu, L. et al. Elucidation of the Sodium Kinetics in Layered P-Type Oxide Cathodes. *Sci. China Chem.* **65**, 2005–2014 (2022).
39. Somerville, J. W. et al. Nature of the "Z"-Phase in Layered Na-Ion Battery Cathodes *Energy*. *Environ. Sci.* **12**, 2223–2232 (2019).
40. Cai, C. et al. Regulating the Interlayer Spacings of Hard Carbon Nanofibers Enables Enhanced Pore Filling Sodium Storage. *Small* **18**, 2105303 (2022).
41. Singh, G. et al. Structural Evolution During Sodium Deintercalation/Intercalation in $Na_{2/3}[Fe_{1/2}Mn_{1/2}]O_2$. *J. Mater. Chem. A* **3**, 6954–6961 (2015).
42. Shi, Y. G. et al. Raman Spectroscopy Study of Na_xCoO_2 and Superconducting $Na_xCoO_2{\cdot}yH_2O$. *Phys. Rev. B* **70**, 052502 (2004).
43. Jiang, N. et al. Tailoring P2/P3 Biphases of Layered Na_xMnO_2 by Co Substitution for High-Performance Sodium-Ion Battery. *Small* **17**, 2007103 (2021).
44. Yang, Z. et al. Superstructure Control of Anionic Redox Behavior in Manganese-Based Cathode Materials for Li-Ion Batteries. *ACS Appl. Mater. interfaces* **14**, 35822–35832 (2022).
45. Kang, S. M. et al. Structural and Thermodynamic Understandings in Mn-Based Sodium Layered Oxides during Anionic Redox. *Adv. Sci.* **7**, 2001263 (2020).
46. Wang, R. et al. A disordered rock-salt Li-excess cathode material with high capacity and substantial oxygen redox activity: $Li_{1.25}Nb_{0.25}Mn_{0.5}O_2$. *Electrochem. Commun.* **60**, 70–73 (2015).
47. Ma, C. et al. Exploring Oxygen Activity in the High Energy P2-Type $Na_{0.78}Ni_{0.23}Mn_{0.69}O_2$ Cathode Material for Na-Ion Batteries. *J. Am. Chem. Soc.* **139**, 4835–4845 (2017).
48. Carroll, K. J. et al. Probing the Electrode/Electrolyte Interface in the Lithium Excess Layered Oxide $Li_{1.2}Ni_{0.2}Mn_{0.6}O_2$. *Phys. Chem. Chem. Phys.* **15**, 11128 (2013).
49. Yang, W. & Devereaux, T. P. Anionic and Cationic Redox and Interfaces in Batteries: Advances from Soft X-ray Absorption Spectroscopy to Resonant Inelastic Scattering. *J. Power Sources* **389**, 188–197 (2018).
50. Shen, Q., Liu, Y., Jiao, L., Qu, X. & Chen, J. Current State-of-the-art Characterization Techniques for Probing the Layered Oxide Cathode Materials of Sodium-Ion Batteries. *Energy Storage Mater* **35**, 400–430 (2021).
51. Ren, H. et al. Unraveling Anionic Redox for Sodium Layered Oxide Cathodes: Breakthroughs and Perspectives. *Adv. Mater.* **34**, 2106171 (2022).
52. Wang, P. et al. Suppressing the P2–O2 Phase Transition of $Na_{0.67}Mn_{0.67}Ni_{0.33}O_2$ by Magnesium Substitution for Improved Sodium-Ion Batteries. *Angew. Chem. Int. Ed.* **55**, 7445–7449 (2016).

53. De la Llave, E. et al. Improving Energy Density and Structural Stability of Manganese Oxide Cathodes for Na-Ion Batteries by Structural Lithium Substitution. *Chem. Mater.* **28**, 9064–9076 (2016).
54. House, R. A. et al. First-Cycle Voltage Hysteresis in Li-Rich 3*d* Cathodes Associated with Molecular O_2 Trapped in the Bulk. *Nat. Energy* **5**, 777–785 (2020).
55. Perdew, J. P., Burke, K. & Ernzerhof, M. Generalized gradient approximation made simple. *Phys. Rev. Lett.* **77**, 3865–3868 (1996).
56. Jain, A. et al. Formation enthalpies by mixing GGA and GGA+Ucalculations. *Phys. Rev. B* **84**, 045115 (2011).
57. Dronskowski, R. & Bloechl, P. E. Crystal orbital Hamilton populations (COHP): energy-resolved visualization of chemical bonding in solids based on density-functional calculations. *J. Phys. Chem.* **97**, 8617–8624 (1993).
58. Deringer, V. L., Tchougréeff, A. L. & Dronskowski, R. Crystal orbital Hamilton population (COHP) analysis as projected from plane-wave basis sets. *J. Phys. Chem. A* **115**, 5461–5466 (2011).
59. Maintz, S., Deringer, V. L., Tchougréeff, A. L. & Dronskowski, R. Analytic projection from plane-wave and PAW wavefunctions and application to chemical-bonding analysis in solids. *J. Comput. Chem.* **34**, 2557–2567 (2013).

Acknowledgements

This work was supported by the National Key Research and Development Program of China (2020YFA0715000, L.M.) and the National Natural Science Foundation of China (U23A20684, L.Z.). This work gratefully acknowledges support from the U.S. Department of Energy (DOE), Office of Energy Efficiency and Renewable Energy, Vehicle Technologies Office. This research used resources of the Advanced Photon Source (beamline 12-BM-B), a U.S. Department of Energy (DOE) Office of Science User Facility, operated for the DOE Office of Science by Argonne National Laboratory under Contract No. DE-AC02- 06CH11357. The STEM was performed at the Nanostructure Research Center (NRC).

Author contributions

C.C., J.L., L.Z., L.M. and K.A. conceived the project, C.C. and X.L. performed the experiments. J.L., L.Z., L.M. and K.A. supervised the projest. C.C., N.X., and H.F. synthesized the materials. R.Y. and J.W. performed the STEM characterizations. P.H. and T.Z. performed the electrochemical testing. J.L., S.L. and T.L. carried out the XANES charaterizations. C.C., X.L., J.L. and L.Z. wroted the paper. All authors discussed the results and reviewed the manuscript. C.C., X.L., J.L. and R.Y. contributed equally to this work.

Competing interests

The authors declare no competing interests.

Additional information

Supplementary information The online version contains supplementary material available at https://doi.org/10.1038/s41467-024-54998-1.

Correspondence and requests for materials should be addressed to Jiantao Li, Liang Zhou, Liqiang Mai or Khalil Amine.

Peer review information *Nature Communications* thanks Se Young Kim, Zulipiya Shadike and the other, anonymous, reviewer for their contribution to the peer review of this work. A peer review file is available.